PHYSICAL REVIEW D **96,** 054002 (2017)

Kaon-nucleon scattering states and potentials in the Skyrme model

Takashi Ezoe[1] and Atsushi Hosaka[1,2]

[1]*Research Center for Nuclear Physics, Osaka University, Ibaraki 567-0048, Japan*
[2]*Advanced Science Research Center, Japan Atomic Energy Agency, Tokai, Ibaraki 319-1195 Japan*
(Received 15 March 2017; revised manuscript received 29 May 2017; published 5 September 2017)

We study the (anti)kaon nucleon interaction in the Skyrme model. The kaon field is introduced as a fluctuation around the rotating Skyrmion for the nucleon. As an extension of our previous work, we study scattering states and examine phase shifts in various kaon-nucleon channels. Then we study the interaction, where we find that it consists of central and spin-orbit components for isospin channels, $I = 0$, 1, with an energy dependence and a nonlocality. The interaction is then fitted to a Shrödinger equivalent local potential for s and p waves.

DOI: 10.1103/PhysRevD.96.054002

I. INTRODUCTION

The antikaon and nucleon ($\bar{K}N$) system is one of the interesting systems in hadron physics. It is considered that the $\bar{K}N$ interaction is strongly attractive. Based on the properties of the $\bar{K}N$ strong attraction, a lot of discussions about the $\bar{K}N$ systems have been done. One example is the $\Lambda(1405)$ resonance known as a candidate of the $\bar{K}N$ quasibound state [1,2], whose properties can not be explained easily by a simple quark model [3]. Another example is the kaonic nucleus, where the antikaon is bound to a nucleus by a strong attraction between them. It is expected that, because of the strong attraction, the structure of the kaonic nucleus is largely modified from normal nuclei [4,5]. In such discussions, the $\bar{K}N$ interaction is obviously the most important input.

In this article, we first discuss the phase shift for both the kaon-nucleon (KN) and $\bar{K}N$ scattering states by a modified bound state approach proposed in the previous work [6]. Our approach is based on the bound state approach, which is proposed by Callan and Klebanov [7,8]. In their original approach, the kaon is introduced as a fluctuation around the hedgehog soliton, and then the kaon-hedgehog system is collectively quantized as hyperons. On the other hand, in our approach, we first generate the nucleon by quantizing the hedgehog soliton, and then introduce the kaon fluctuation around the physical nucleon. There are works for (anti)kaon-nucleon scatterings in the Skyrme model [9,10]. In these works, (anti) kaon fluctuations were introduced around the Skyrmion background, which corresponds to the Callan-Klebanov approach [7,8]. The difference between the Callan-Klebanov and our approaches is in the order of the projection and variation. The Callan-Klebanov approach corresponds to the projection after variation, while ours to the variation after projection. In the previous paper, we have investigated $\bar{K}N$ bound states. As a result, we found one bound state for the $\bar{K}N(J^P = 1/2^-, I = 0)$ channel with a binding energy of an order of 10 MeV corresponding to $\Lambda(1405)$.

Secondly, we derive a Schrödinger equivalent local potential for the (anti)kaon and nucleon. The resulting potential is fitted by Gaussian type functions, which are convenient for the study of few-body nuclear systems with the antikaon. In general, the (anti)kaon-nucleon potential has four components: the isospin independent and dependent central terms, and the spin-orbit terms (LS terms). These complete all the possible components for the pseudoscalar and isoscalar (anti)kaon and the spinor and isospinor nucleon. Furthermore, the interaction is energy dependent and nonlocal.

We organize the paper as follows. In the next section, we briefly review our approach, which we have constructed in the previous work. In Sec. III, we discuss the phase shifts for (anti)kaon nucleon scattering states with lower (anti) kaon partial waves. In Sec. IV, we derive various components of the potential and perform a fitting to Gaussian type functions. Then, we discuss the scaling properties of the potential associated with the scaling properties of soliton solutions. In the end, we summarize the present work and discuss further studies.

II. FORMALISM

In this section, we review our modified bound state approach. Detailed discussions have been done in Ref. [6]. Let us start with the following action for the SU(3)-valued field $U = U(r)$:

$$\Gamma = \int d^4x \left\{ \frac{1}{16} F_\pi^2 \mathrm{tr}(\partial_\mu U \partial^\mu U^\dagger) + \frac{1}{32e^2} \mathrm{tr}[(\partial_\mu U)U^\dagger, (\partial_\nu U)U^\dagger]^2 + L_{SB} \right\} + \Gamma_{WZ}, \quad (1)$$

where the first and second terms are the Skyrme actions [11–13] and the third term is the symmetry breaking term due to the finite masses of the SU(3) pseudoscalar mesons with [14,15]

$$L_{SB} = \frac{1}{48} F_\pi^2 (m_\pi^2 + 2m_K^2) \mathrm{tr}(U + U^\dagger - 2) + \frac{\sqrt{3}}{24} F_\pi^2 (m_\pi^2 - m_K^2) \mathrm{tr}[\lambda_8 (U + U^\dagger)]. \quad (2)$$

In this paper, we treat the pion as a massless particle while the kaon as massive one. We call the three terms in Eq. (1) as normal terms in this paper. The last term in Eq. (1) is the contribution of the chiral anomaly called the Wess-Zumino term given by [16–18]

$$\Gamma_{WZ} = -\frac{iN_c}{240\pi^2} \int d^5 x \epsilon^{\mu\nu\alpha\beta\gamma} \times \mathrm{tr}[(U^\dagger \partial_\mu U)(U^\dagger \partial_\nu U)(U^\dagger \partial_\alpha U)(U^\dagger \partial_\beta U)(U^\dagger \partial_\gamma U)], \quad (3)$$

where N_c is the number of colors, $N_c = 3$.

The flavor SU(3) symmetry breaking is reflected in the difference of both the masses and the decay constants of the SU(3) pseudoscalar mesons [19–21]. Because in the present study, the η-meson is irrelevant, we have two decay constants F_π and F_K. Experimentally, they differ only by about 20%, and therefore, we will take a common value of them, typically their average. The use of the different values of F_π and F_K will be discussed shortly in the next section. Therefore, the action Eq. (1) contains three parameters: the pion decay constant, F_π, the Skyrme parameter, e, and the mass of the (anti)kaon, m_K. Here, we keep m_K at the experimental value, 495 MeV, and we consider three parameter sets for F_π and e. We will show them in the next section.

To study the interaction of the kaon with the physical nucleon, we introduce the ansatz,

$$U = A(t) \sqrt{U_\pi} A^\dagger(t) U_K A(t) \sqrt{U_\pi} A^\dagger(t), \quad (4)$$

where $A(t)$ is an isospin rotation matrix, U_π is the hedgehog pion field with the soliton profile function, $F(r)$,

$$U_\pi = \begin{pmatrix} \xi^2 & 0 \\ 0 & 1 \end{pmatrix}, \qquad \xi^2 = \exp[iF(r) \boldsymbol{\tau} \cdot \hat{\boldsymbol{r}}], \quad (5)$$

and

$$U_K = \exp\left[\frac{2\sqrt{2}i}{F_\pi} \begin{pmatrix} 0 & K \\ K^\dagger & 0 \end{pmatrix} \right], \qquad K = \begin{pmatrix} K^+ \\ K^0 \end{pmatrix}. \quad (6)$$

As discussed in Ref. [6], the ansatz Eq. (4) describes the kaon fluctuation around the rotating hedgehog soliton, and differs from the ansatz of Callan and Klebanov for the kaon around the static hedgehog soliton [7,8]. Therefore, in our approach, the system describes the physical (anti)kaon and nucleon. Contrary, in the Callan-Klebanov approach, the antikaon around the background hedgehog soliton behaves as an s quark after collective quantization.

Now we derive the equation of motion for the kaon field. To do that, we first substitute our ansatz Eq. (4) for the action Eq. (1), and then we expand U_K up to the second order of the kaon field, K. As a result, we obtain the following Lagrangian for the kaon-nucleon system:

$$L = L_{SU(2)} + L_{KN}, \quad (7)$$

$$\begin{aligned} L_{KN} = {} & (D_\mu K)^\dagger D^\mu K - K^\dagger a_\mu^\dagger a^\mu K - m_K^2 K^\dagger K \\ & + \frac{1}{(eF_\pi)^2} \{ -K^\dagger K \mathrm{tr}[\partial_\mu \tilde{U} \tilde{U}^\dagger, \partial_\nu \tilde{U} \tilde{U}^\dagger]^2 \\ & - 2(D_\mu K)^\dagger D_\nu K \mathrm{tr}(a^\mu a^\nu) \\ & - \frac{1}{2} (D_\mu K)^\dagger D^\mu K \mathrm{tr}(\partial_\nu \tilde{U}^\dagger \partial^\nu \tilde{U}) + 6 (D_\nu K)^\dagger [a^\nu, a^\mu] D_\mu K \} \\ & + \frac{3i}{F_\pi^2} B^\mu [(D_\mu K)^\dagger K - K^\dagger (D_\mu K)], \end{aligned} \quad (8)$$

where the covariant derivative is defined as $D_\mu = \partial_\mu + v_\mu$, and the vector and axial vector currents are

$$v_\mu = \frac{1}{2} (\tilde{\xi}^\dagger \partial_\mu \tilde{\xi} + \tilde{\xi} \partial_\mu \tilde{\xi}^\dagger), \quad (9)$$

$$a_\mu = \frac{1}{2} (\tilde{\xi}^\dagger \partial_\mu \tilde{\xi} - \tilde{\xi} \partial_\mu \tilde{\xi}^\dagger). \quad (10)$$

In these equations, the tilded quantities are rotating,

$$\tilde{U} = A(t) \xi^2 A^\dagger(t), \qquad \tilde{\xi} = A(t) \xi A^\dagger(t), \quad (11)$$

as required by our ansatz Eq. (4). Finally, the last term of Eq. (8) is derived from the Wess-Zumino term with the baryonic current [22], B_μ.

Next, we decompose the kaon field into the two-component isospinor and spatial wave functions, and expand the latter into partial waves by the spherical harmonics, $Y_{lm}(\hat{r})$,

$$\begin{pmatrix} K^+ \\ K^0 \end{pmatrix} = \psi_I K(t, \boldsymbol{r}) \to \psi_I K(\boldsymbol{r}) \exp(-iEt), \quad (12)$$

$$K(\boldsymbol{r}) = \sum_{\alpha l m} C_{lm\alpha} Y_{lm}(\hat{r}) k_l^\alpha(r), \quad (13)$$

where ψ_I is the two component isospinor.

Finally, taking a variation with respect to the kaon wave function, we obtain the equation of motion for each partial wave, $k_l^\alpha(r)$,

$$-\frac{1}{r^2}\frac{d}{dr}\left(r^2 h(r)\frac{dk_l^\alpha(r)}{dr}\right) - E^2 f(r) k_l^\alpha(r) + (m_K^2 + V(r))k_l^\alpha(r) = 0, \quad (14)$$

where $h(r)$ and $f(r)$ are functions depending on the profile function, $F(r)$, and E is the energy of the kaon including the rest mass of the kaon. The last term in Eq. (14), $V(r)$, is the (anti)kaon-nucleon interaction term. In Appendix A, we show explicit forms of each term in Eq. (14).

III. SCATTERING STATES

Let us first discuss the model parameters. As we mentioned in the previous section, in this paper, we consider three parameter sets for F_π and e as shown in the Table I. These parameter sets reproduce the same moment of inertia such that the mass splitting of the nucleon and delta becomes the physical value. Further explanations are as follows:

(i) Parameter set A: we employ the pion decay constant slightly larger than the physical one. This is motivated by the facts that the kaon decay constant, F_K, is larger than the pion one ($F_K = 221$ MeV [23]) and that we are interested in a physical system of the pion and kaon. Therefore, we choose $F_\pi = 186 \times 1.1 = 205$ MeV. The Skyrme parameter, e, is then fixed to reproduce the $N\Delta$ mass splitting together with the above F_π value. The reason that we use an experimentally inspired value for the decay constant is that it determines the interaction strength of the pion (kaon) and nucleon. As the Tomozawa-Weinberg theorem says, the choice of the experimental value is needed to explain the pion-nucleon scattering length [24,25]. For the Skyrme parameter e, the present value overestimates the absolute masses of the nucleon and delta. However, these masses are subject to the correction from the Casimir energy of order $(1/N_c^0)$ which reduces their large masses [26,27].

(ii) Parameter set B: this is adjusted to fit the $N\Delta$ mass splitting with F_π fixed at the experimental value.

(iii) Parameter set C: this is proposed by Adkins, Nappi, and Witten [22], which reproduces the observed masses of the nucleon and the delta.

For the parameter set A, there is one bound state for the $I = 0$ channel with the binding energy 20.6 MeV while, for the $I = 1$ channel, no bound state exists. There is one bound state for the $I = 0$ and $I = 1$ channels with the sets B and C [28]. For the KN channel, the kaon and nucleon does not form a bound state due to the strong repulsion by the Wess-Zumino term for the three parameter sets.

TABLE I. Parameter sets and binding energy (B.E.).

	F_π [MeV]	e	B.E. [MeV]
Parameter set A	205	4.67	20.6
Parameter set B	186	4.82	32.2
Parameter set C	129	5.45	81.3

In addition to the three parameter sets, A, B, and C, we have considered another one with different decay constants: $F_K = 221$ MeV, $F_\pi = 186$ MeV, and $e = 4.82$. Here, the Skyrme parameter $e = 4.82$ has been determined such that the $N\Delta$ mass splitting is reproduced as before. Then we have found similar results both for bound and scattering state properties to those in the parameter set A. For instance, the binding energy of the $\bar{K}N(I = 0)$ system turns out to be 17.6 MeV. The difference of F_π and F_K due to the flavor SU(3) symmetry breaking is important for more quantitative discussions. In that case, we also need to consider other issues such as the explicit chiral symmetry breaking of the finite pion mass. In the present work, however, we consider a simple case as a first attempt for the study of the essential features of the kaon and nucleon systems.

Now, we show the results for the scattering states. We have calculated the phase shifts for the s- and p-wave (anti) kaon nucleon scattering states for all of the parameter sets. However, for the realistic situations of the (anti)kaon and nucleon systems, it turns out that the use of the physical pion decay constant is important. Therefore, in the following discussions, we will present in most cases the results of using the parameter sets A and B.

First, we show in Fig. 1 phase shifts for s-wave scatterings with various channels as functions of the kinetic energy ε, which is defined by $E = m_K + \varepsilon$. For the set A (left), the phase shift of the $\bar{K}N(I = 0)$ channel starts from π at $\varepsilon = 0$, reflecting the fact that there is one bound state. For the $\bar{K}N(I = 1)$ channel, there is not a bound state but it shows an attractive nature as the positive phase shifts indicate. For the KN scattering, both $I = 0$ and $I = 1$ channels are weakly repulsive but the $I = 1$ channel is stronger.

For the set B (right), $\bar{K}N$ channels allow a bound state for both $I = 0$ and $I = 1$. The bound state of $I = 1$ is, however, very shallow indicating that the attractive interaction is weaker than in the $I = 0$ channel. The $I = 1$ bound state disappears by slightly increasing the pion decay constant as chosen in the parameter set A. We may further attempt fine-tuning of the parameters, but we will not do this because our present model contains only KN channels. Physically, the inclusion of the $\pi\Sigma$ channels is very important, which we will do in the future.

From Fig. 1, we find that the strength of the repulsion for KN and the attraction for $\bar{K}N$ are stronger for the set B than for the set A. This reflects the fact that the obtaining potential is approximately proportional to $1/F_\pi^2$ as the Weinberg-Tomozawa theorem implies [24,25].

To complete the discussions up to here, we show the phase shifts for all parameter sets A, B, and C for the

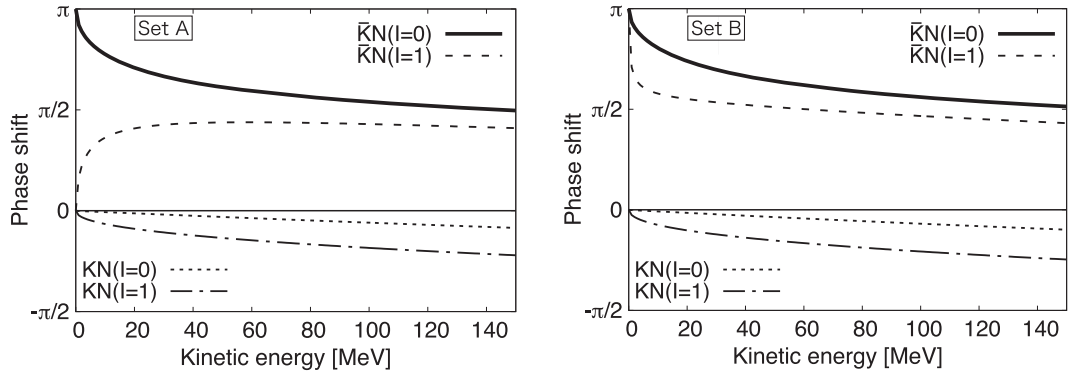

FIG. 1. Phase shifts for the (anti)kaon-nucleon scattering state with $J^P = 1/2^-$ for the parameter sets A (left) and B (right).

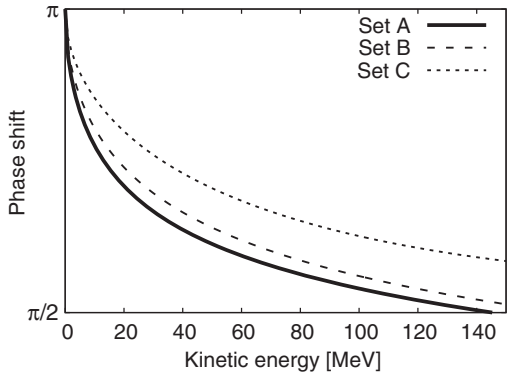

FIG. 2. The phase shifts for the $\bar{K}N(J^P = 1/2^-, I = 0)$ channel with the three parameter sets A, B, and C.

$\bar{K}N(J^P = 1/2^-, I = 0)$ channel in Fig. 2. In this figure, we can find that the attraction between the antikaon and the nucleon becomes stronger in the order of the set A, B, and C, which is consistent with the properties of the $\bar{K}N$ bound states shown in Table. I.

Next, in Fig. 3, we have shown the phase shifts for p waves, first for $J^P = 3/2^+$ channels. In both sets A and B, the phase shifts show the attractive and repulsive behaviors for the $\bar{K}N$ and KN channels, respectively. However, the strength of them are weaker than those of the s wave. The phase shifts in the $\bar{K}N$ channels show that the $I = 1$ channel is more attractive than the $I = 0$ one due to the stronger isospin-dependent LS force in the $I = 1$ channel.

For the other LS partner of $J^P = 1/2^+$ channel, the interaction shows a strong attraction as proportional to $1/r^2$. Because of this, the system becomes unstable and physically meaningful solutions are not allowed. We consider that it is related to the hedgehog structure, but the physical meaning is not yet clarified.

Finally, let us evaluate the scattering length, a, for the $\bar{K}N(J^P = 1/2^-)$ scattering state, which is defined by

$$a = -\lim_{k\to 0} \frac{\tan\delta(k)}{k}, \tag{15}$$

where k is the wave number and $\delta(k)$ is the phase shift. From this equation, we have obtained $a_0 = 1.56$ fm and $a_1 = -3.38$ fm for the $\bar{K}N$ scattering with isospin 0 and 1 channels, respectively, for the set A. As a result, we have $a_{\bar{K}N} = -0.91$ fm as the $\bar{K}N$ scattering length with the parameter set A.

For the set B, we have obtained $a_0 = 1.32$ fm and $a_1 = 8.22$ fm for the $\bar{K}N(I = 0, 1)$ scatterings. We find that a_0 for the set A is longer than that for the set B, while a_1 changes its sign and the absolute value of it is shorter for the set A than for the set B. This is because the attraction

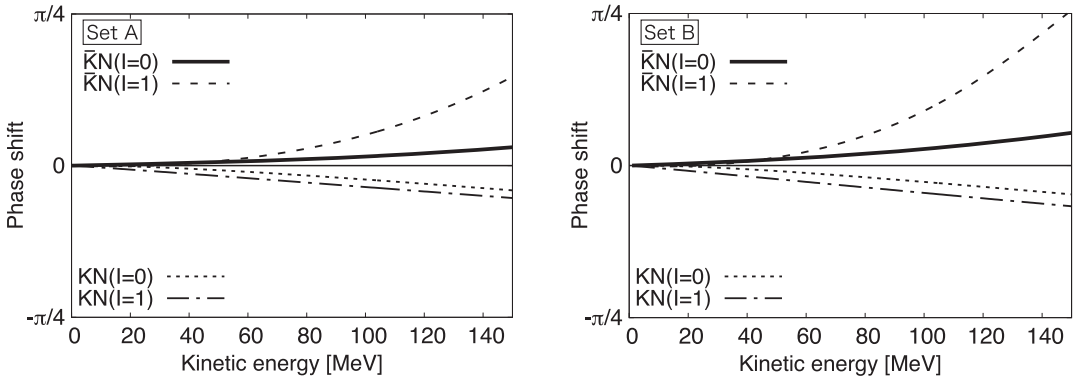

FIG. 3. Phase shifts for the (anti)kaon-nucleon scattering state with $J^P = 3/2^+$ for the parameter sets A (left) and B (right).

between $\bar{K}$ and N for the set B is stronger than that for the set A.

All the scattering lengths derived here are real. However, those obtained from experiments and other theoretical calculations are complex [29–33]. The reason is that we do not consider the coupled channel effect of the $\pi\Sigma$ channel, which is needed for a more realistic comparison. Because of this, in the present paper, we will not make further quantitative discussions.

IV. POTENTIAL

In this section, we investigate the $\bar{K}N$ potential in detail. Numerical results are then fitted to a simple functional form, which is useful for various applications to the study of $\bar{K}$-nucleon systems. First, we consider the potential for the parameter set A. For the sets B and C, we discuss them with scaling rules from the set A to the sets B and C.

A. Derivation and classification of the potential

Let us start with the equation of motion Eq. (14) in the following Schrödinger-like form with the potential $U(r)$ in units of MeV:

$$-\frac{1}{m_K+E}\frac{1}{r^2}\frac{d}{dr}\left(r^2\frac{dk_l^\alpha(r)}{dr}\right)+U(r)k_l^\alpha(r)=\varepsilon k_l^\alpha(r), \tag{16}$$

where $E=m_K+\varepsilon$, and

$$U(r)=-\frac{1}{m_K+E}\left[\frac{h(r)-1}{r^2}\frac{d}{dr}\left(r^2\frac{d}{dr}\right)+\frac{dh(r)}{dr}\frac{d}{dr}\right] -\frac{(f(r)-1)E^2}{m_K+E}+\frac{V(r)}{m_K+E}. \tag{17}$$

The potential $U(r)$ has the following properties [6]: it is nonlocal and depends on the energy of the kaon. Second, it contains isospin independent and dependent central terms and spin-orbit (LS) terms. Finally, there are repulsive components proportional to $1/r^2$ at short distances.

Because this expression contains the derivative operators, we define the equivalent local potential $\tilde{U}(r)$ with the kaon partial wave function, $k_l^\alpha(r)$,

$$\tilde{U}(r)\equiv\frac{U(r)k_l^\alpha(r)}{k_l^\alpha(r)}. \tag{18}$$

This definition, however, can not be used when the wave function becomes zero at nodal points. We may avoid this problem by using a bound state for the $\bar{K}N(I=0)$ channel, which allows one bound state, and for the other channels, by using a scattering state with a small energy such that the first node of the wave function appears at a large r, where the potential is sufficiently suppressed. In the following, we show the results for the scattering energy $\varepsilon=27$ MeV, while we have confirmed that results do not change as long as the scattering energy is small.

As mentioned already, the equivalent local potential $\tilde{U}(r)$ has four kinds of components. Here, we decompose them further into seven components reflecting different origins of the potential,

$$\begin{aligned}\tilde{U}(r)=&\tilde{U}_0^c(N,r)+\tilde{U}_\tau^c(N,r)I_{KN}\\&+\tilde{U}_0^{LS}(N,r)J_{KN}+\tilde{U}_\tau^{LS}(N,r)J_{KN}I_{KN}\\&+\tilde{U}_0^c(WZ,r)+\tilde{U}_0^{LS}(WZ,r)J_{KN}+\tilde{U}_l(r),\end{aligned} \tag{19}$$

where superscripts, c and LS, stand for the central and spin-orbit (LS) forces, respectively, and subscripts, 0 and τ, are for isospin independent and dependent components, respectively. The arguments, N and WZ, indicate the terms derived from the normal terms of the Skyrme Lagrangian and the Wess-Zumino term, respectively. In Eq. (19), we have defined I_{KN} and J_{KN} as $I_{KN}=\boldsymbol{I}^K\cdot\boldsymbol{I}^N$ and $J_{KN}=\boldsymbol{L}^K\cdot\boldsymbol{J}^N$, respectively. The former, I_{KN}, corresponds to the product of the isospin operator for the kaon and the nucleon and the latter, J_{KN}, to the product of the angular momentum of the kaon and the spin of the nucleon. The last term in Eq. (19), $\tilde{U}_l(r)$, is the centrifugal force of the kaon. Because the Wess-Zumino term corresponds physically to the ω-meson exchange, that is the isoscalar particle exchange [16–18,34], it has no isospin dependent contributions in Eq (19).

The seven potential components have energy dependence, for which we make a linear approximation in terms of $\Delta_E\equiv\varepsilon/2m_K$,

$$\begin{aligned}\tilde{U}(r)&\simeq\tilde{U}(r)+\frac{\partial\tilde{U}(r)}{\partial\varepsilon}\Delta_E\\&\equiv u(r)+v(r)\Delta_E.\end{aligned} \tag{20}$$

We then fit all the components of $u(r)$ and $v(r)$ by several Gaussian type functions,

$$G_{-2}(r)=C_{-2}\frac{1}{r^2/{R_{-2}}^2}\exp\left(-\frac{r^2}{{R_{-2}}^2}\right) \tag{21}$$

$$G_0(r)=C_0\exp\left(-\frac{r^2}{{R_0}^2}\right) \tag{22}$$

$$G_2(r)=C_2\frac{r^2}{{R_2}^2}\exp\left(-\frac{r^2}{{R_2}^2}\right), \tag{23}$$

as summarized in Table II. For example, the isospin independent components of the central terms derived from the normal Skyrme Lagrangian, $u_0^c(N,r)$ and $v_0^c(N,r)$, are fitted by the three functions, $G_{-2}(r)$, $G_0(r)$, and $G_2(r)$. The first one, $G_{-2}(r)$, is the Gaussian divided by r^2, which

TABLE II. Various components of the $\bar{K}N$ potential and the corresponding fitted functions. The functions $u(r)$ and $v(r)$ are for energy independent and dependent components with upper and lower indices as explained in the text. The fitted functions $G_n(r)$ are also defined in the text, Eqs. (21), (22), and (23). Superscripts, (1) and (2) of $G_n^{(\cdot)}(r)$, indicate that the fitting parameters are different for the functions.

	Isospin	Fitting function
Central	independent	$u_0^c(N,r)+v_0^c(N,r)\Delta_E$
		$G_{-2}(r)+G_0(r)+G_2(r)$
		$u_0^c(WZ,r)+v_0^c(WZ,r)\Delta_E$
		$G_0^{(1)}(r)+G_0^{(2)}(r)$
	dependent	$u_\tau^c(N,r)+v_\tau^c(N,r)\Delta_E$
		$G_0(r)+G_2(r)$
LS	independent	$u_0^{LS}(N,r)+v_0^{LS}(N,r)\Delta_E$
		$G_0^{(1)}(r)+G_0^{(2)}(r)$
		$u_0^{LS}(WZ,r)+v_0^{LS}(WZ,r)\Delta_E$
		$G_0^{(1)}(r)+G_0^{(2)}(r)$
	dependent	$u_\tau^{LS}(N,r)+v_\tau^{LS}(N,r)\Delta_E$
		$G_{-2}^{(1)}(r)+G_{-2}^{(2)}(r)$
Centrifugal force		$u_l(r)+v_l(r)\Delta_E$
		$[G_0^{(1)}(r)+G_0^{(2)}(r)+1]/2m_Kr^2$

is needed to reproduce a repulsive behavior in the short range, and the second and third are the Gaussians with the polynomial of r^0 and r^2.

For the centrifugal term, we have fitted as follows:

$$\tilde{U}_l(r)=\frac{l(l+1)}{2m_Kr^2}[G_0^{(1)}(r)+G_0^{(2)}(r)+1], \quad (24)$$

where l and m_K are the angular momentum and the mass of the kaon, respectively. At short and middle distances, the centrifugal term deviates from the ordinary one of $1/r^2$ due to background fields of the hedgehog soliton. However, at long distances, it reduces to the ordinary form.

As mentioned in the Introduction, the Gaussian functional form is convenient for practical applications. However, its functional form falls off much faster than the actual functional form that falls off only by the inverse polynomial power of the radial distance r for the massless pion Skyrmion. The difference at large distances, however, does not affect the properties of the (anti)kaon-nucleon systems.

B. Numerical fitting

In this subsection, we compare numerically obtained potentials with those fitted by the Gaussian forms for each component in Figs. 4–10. The fitting parameters are shown in Tables III–IX in Appendix B.

We have treated both ranges, R_i, and strengths, C_i, as fitting parameters. Practically, we have performed the fitting as follows: first, we have fitted both range and strength parameters for the energy independent components because they are the dominant contributions. Then, we have determined the strength parameters of the energy dependent components with the same range parameters as the energy independent ones. This is because we consider that the energy independent and dependent components have the same physical origin, if based on a boson exchange picture.

Let us now make detailed discussions for each component below. We concentrate on the $\bar{K}N$ potentials but we can estimate the KN ones with taking into account the difference of the quantum numbers. However, due to the nonlocality, we need to solve the equation of motion to derive more accurate potentials.

From Figs. 4–10, we can see that the fitting is done by the Gaussian forms in a good manner. We find that four components, $U_0^c(WZ,r)$, $U_0^{LS}(N,r)$, $U_0^{LS}(WZ,r)$, and $U_\tau^{LS}(N,r)$, are fitted by a single Gaussian function, $G_0(r)$ or $G_{-2}(r)$, but with different ranges that are indicated by the superscript, while the others, $U_0^c(N,r)$, $U_\tau^c(N,r)$, and $U_l(r)$, are fitted with the different forms. We consider that the reason behind this is that the former originates from a simple physical mechanism while the latter from a complex one.

From now on, we make discussions for each component below.

(i) Figure 4

For the s-wave channel, as shown in the upper left panel, we find that there is an attractive pocket whose depth is around 100 MeV in the middle range and a repulsive core at a short distances in the energy independent potential, $u_0^c(N,r)$. Contrary, the energy dependent components, $v_0^c(N,r)$, behave rather monotonically with an attraction as proportional to $1/r^2$. Turning to the p-wave potential as shown in the lower panel, an energy independent component is attractive as it is proportional to $1/r^2$, while the energy dependent one behaves similarly to the s-wave energy independent component, but with a shorter range. We can also see that the energy independent and dependent components behave in a quite different manner between the s- and p-wave channels. This is because of the nonlocal contributions of them. To see that, we first separate the potentials, $u_0^c(N,r)$ and $v_0^c(N,r)$, into the local and nonlocal contributions for the two channels,

$$u_0^c(N,r)=u_0^c(N,\mathrm{local},r)+u_0^c(N,\mathrm{non},r) \quad (25)$$

$$v_0^c(N,r)=v_0^c(N,\mathrm{local},r)+v_0^c(N,\mathrm{non},r), \quad (26)$$

where the arguments local and non stand for the local and nonlocal contributions, respectively. Then,

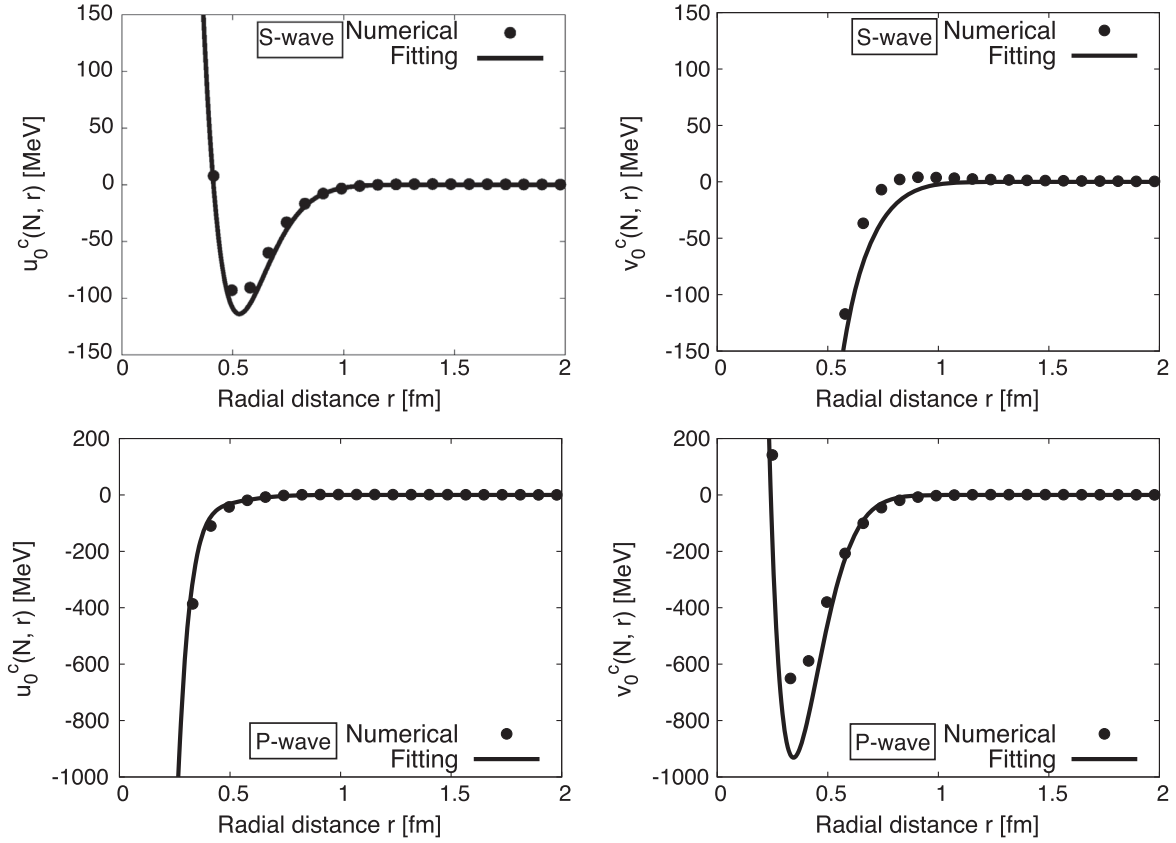

FIG. 4. Comparisons between the numerically obtained and the Gaussian-fitted potentials for $u_0^c(N, r)$ (left) and $v_0^c(N, r)$ (right) for the s-wave (upper panels) and p-wave (lower panels) components.

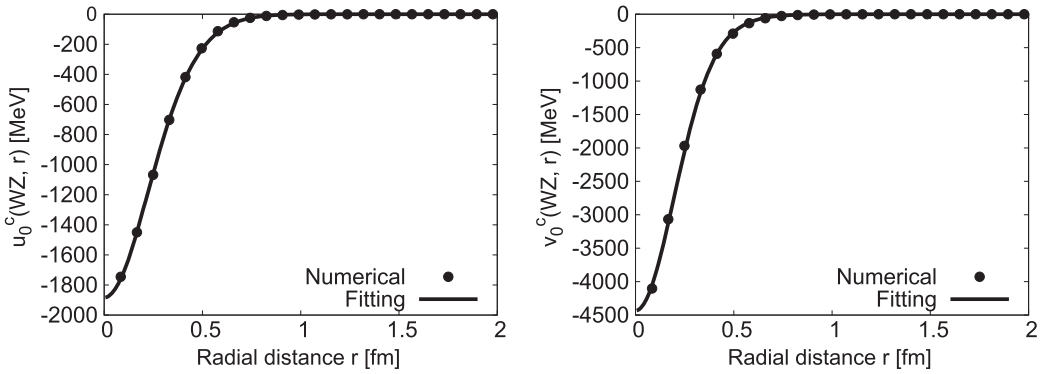

FIG. 5. Comparisons between the numerically obtained and the Gaussian-fitted potentials for $u_0^c(WZ, r)$ (left) and $v_0^c(WZ, r)$ (right).

we have numerically calculated the nonlocal contributions for the s and p waves and shown the results in Fig. 11, where the s-wave components are plotted by a solid line and the p-wave one by a dashed line. We can see that the nonlocal contributions are quite different between them.

Because the local potential strongly depends on the state as shown in Fig. 11, we need to derive the local potentials for the state by state in order to obtain more accurate ones. Therefore, for more practical uses, we decompose $u_0^c(N, r)$ and $v_0^c(N, r)$ into the local and nonlocal components and then fit the local components and the coefficients of the derivative operators. Details of this fitting are done in Appendix C.

(ii) Figure 5

We can see that the energy independent and dependent components behave in a similar way but their strengths are very much different. To see this, the contribution is expanded with respect to $\Delta_E = \varepsilon/2m_K$ as in Eq. (20),

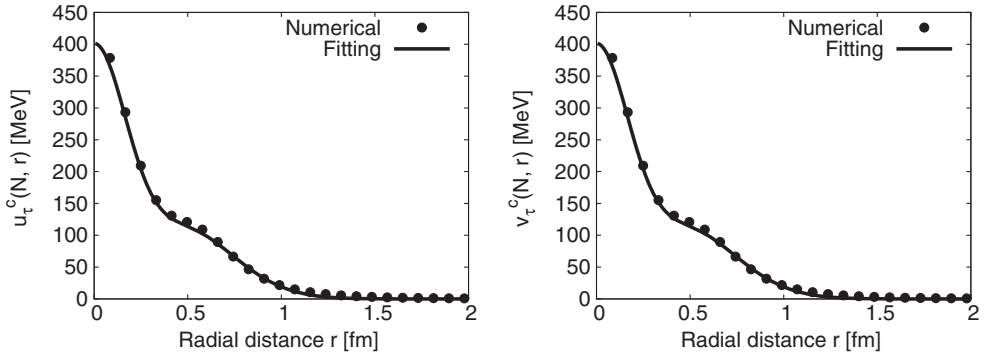

FIG. 6. Comparisons between the numerically obtained and the Gaussian-fitted potentials for $u_\tau^c(N,r)$ (left) and $v_\tau^c(N,r)$ (right).

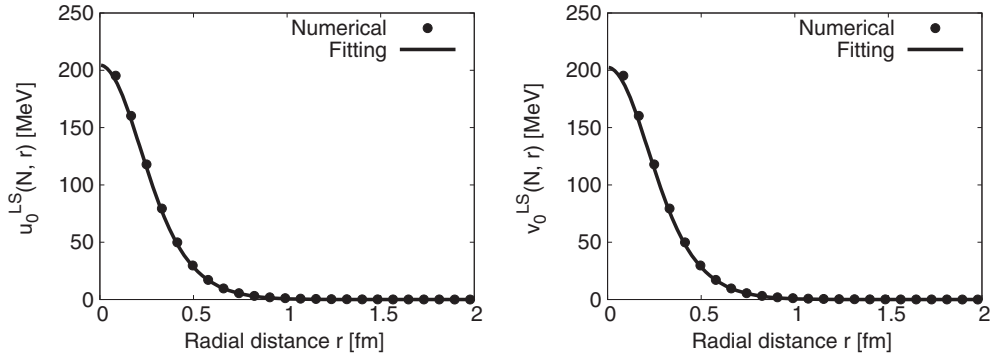

FIG. 7. Comparisons between the numerically obtained and the Gaussian-fitted potentials for $u_0^{LS}(N,r)$ (left) and $v_0^{LS}(N,r)$ (right).

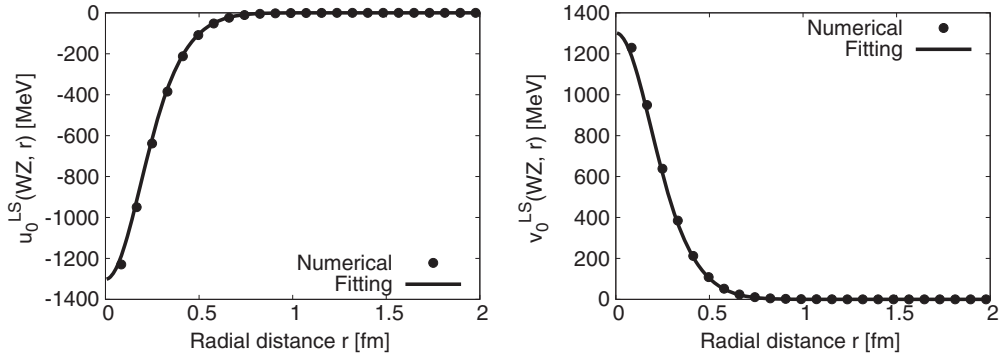

FIG. 8. Comparisons between the numerically obtained and the Gaussian-fitted potentials for $u_0^{LS}(WZ,r)$ (left) and $v_0^{LS}(WZ,r)$ (right).

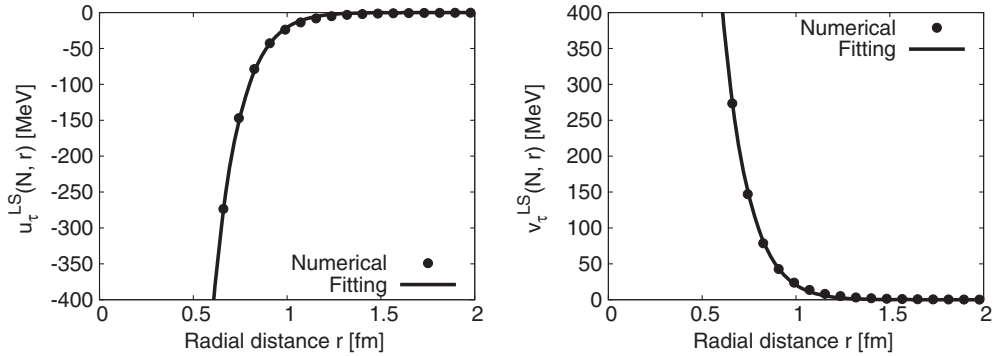

FIG. 9. Comparisons between the numerically obtained and the Gaussian-fitted potentials for $u_\tau^{LS}(N,r)$ (left) and $v_\tau^{LS}(N,r)$ (right).

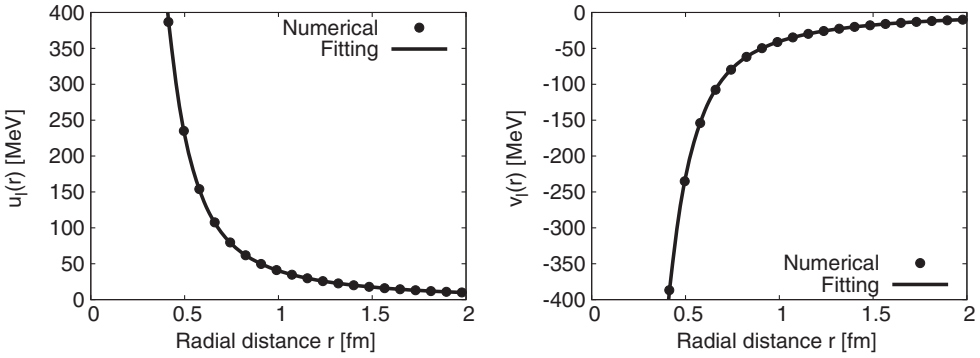

FIG. 10. Comparisons between the numerically obtained and the Gaussian-fitted potentials for $u_l(r)$ (left) and $v_l(r)$ (right).

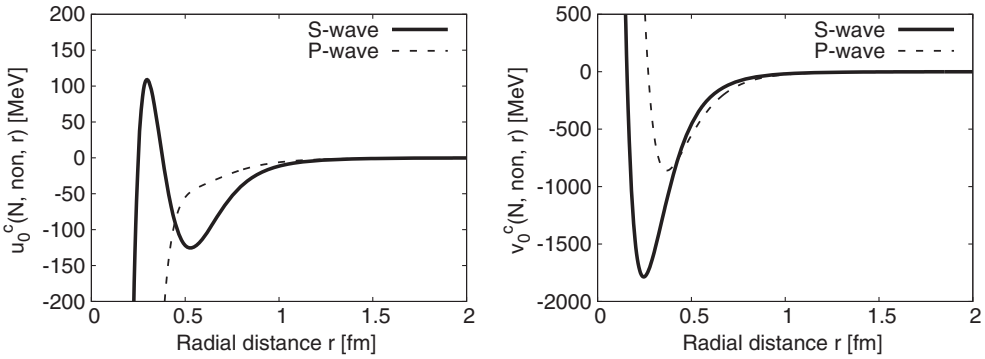

FIG. 11. Nonlocal components of $u_0^c(N,r)$ (left) and $v_0^c(N,r)$ (right) for the s and p waves (solid and dashed lines, respectively).

$$U_0^c(WZ,r) = \frac{1}{m_K+E}\frac{3}{\pi^2 F_\pi^2}\frac{\sin^2 F}{r^2}F'\left(E-\frac{s^2}{\Lambda}\right) \propto \frac{1}{m_K+E}\left(E-\frac{s^2}{\Lambda}\right) \simeq \left(\frac{1}{2}-\frac{1}{2m_K}\frac{s^2}{\Lambda}\right)+\left(\frac{1}{2}+\frac{1}{2m_K}\frac{s^2}{\Lambda}\right)\Delta_E, \tag{27}$$

where the explicit expressions of $U_0^c(WZ,r)$ are shown in Eq. (A9). In Eq. (27), Λ is a moment of inertia of the SU(2) hedgehog soliton, and we define $s=\sin(F(r)/2)$. In our definition for $u_0^c(WZ,r)$ and $v_0^c(WZ,r)$, the first and second terms in Eq. (27) correspond to $u_0^c(WZ,r)$ and $v_0^c(WZ,r)$, respectively. Therefore, we obtain the following relations:

$$u_0^c(WZ,r) \propto \frac{1}{2}-\frac{1}{2m_K}\frac{s^2}{\Lambda} \tag{28}$$

and

$$v_0^c(WZ,r) \propto \frac{1}{2}+\frac{1}{2m_K}\frac{s^2}{\Lambda}. \tag{29}$$

From these equations, we find that the difference of the energy independent and dependent terms of the Wess-Zumino term is proportional to s^2/Λ. This explains the difference in the strengths shown in Fig. 5.

(iii) Figures 6 and 7
In these figures, it is shown that the energy independent and dependent components become exactly the same. This should have been expected from the analytic form of the potential as shown in Eqs. (A10) and (A11), from which we can read explicitly,

$$u(r) = v(r). \tag{30}$$

(iv) Figures 8, 9, and 10
We can see that the strengths of the potentials are the same for each component but the sign is different between the energy independent and dependent components. We can easily verify it from their explicit forms shown in Appendix A.

Finally, we show the total potentials, which are numerically obtained and fitted by the Gaussian forms in Fig. 12. For the s-wave potential, we can see a repulsion at the short distances, which comes from the isospin independent central term of the normal Skyrme Lagrangian, $U_0^c(N,r)$, as shown in Fig. 4. In the middle range, we find an attractive pocket, which may generate the bound state. From Figs. 4–6, this attractive pocket is dominantly made by the attraction of the Wess-Zumino term.

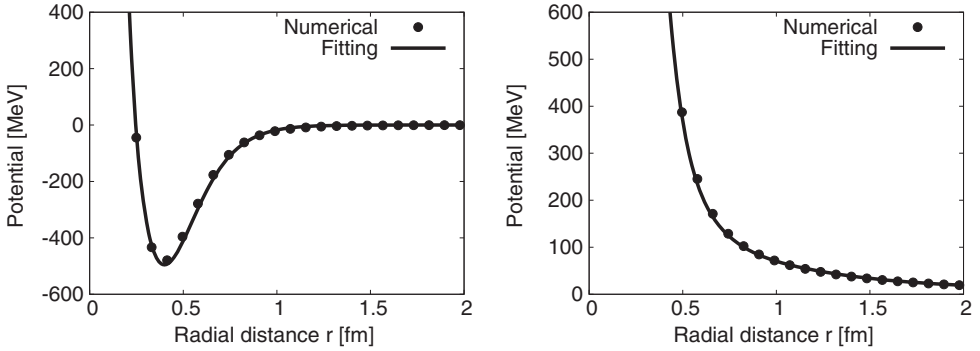

FIG. 12. Total potentials for the $\bar{K}N(J^P = 1/2^-, I = 0)$ channel obtained from the bound state (left) and those for the $\bar{K}N(J^P = 3/2^+, I = 0)$ channel from a scattering state (right).

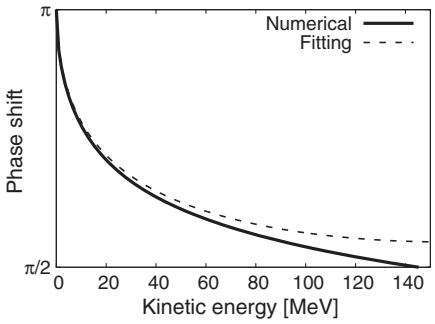

FIG. 13. The phase shifts for the $\bar{K}N(J^P = 1/2^-, I = 0)$ channel obtained from the numerical and fitted potentials with the set A.

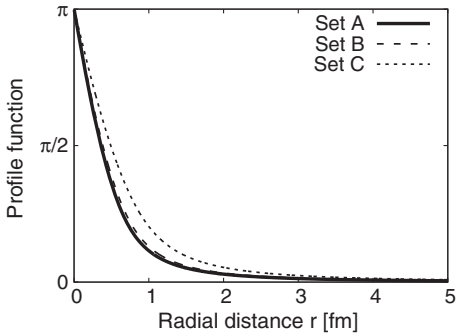

FIG. 14. The profile functions $F(r)$ for the three parameter sets A, B, and C.

From Fig. 12, we see that the behaviors of the potentials for the s wave $(1/2^-)$ and p wave $(3/2^+)$ are different; an attractive pocket vanishes for the p wave. This is due to the strong repulsion of the LS and centrifugal components from the normal term.

So far we have seen that the fitting of the potential works well, particularly for the local terms, while that for the nonlocal terms is not always the case as Fig. 11 shows. The nonlocal terms induce also energy dependence. To see this point, we check how the phase shifts are reproduced by the fitted potential as functions of the kinetic energy. In Fig. 13, we have compared the phase shifts calculated by the numerically obtained and fitted potentials. In the low energy region $(\varepsilon \lesssim 50$ MeV), where we consider that our approach works well, the two phase shifts agree well. Contrary, as the kinetic energy is getting larger, the difference of the phase shifts becomes larger, which is due to the nonlocal contributions. Therefore, our fitted potential can be used for practical calculations for low energy (anti)kaon and nucleon systems.

C. Scaling rules

So far, we have performed the potential fitting for the parameter set A. In this subsection, we consider it for the sets B and C by using the scaling property of the Skyrmion. In this way, various properties of the interaction will be better understood. First, we briefly review the scaling rule in the Skyrme model and then show the scaling rules for the fitting parameters. Finally, we compare the numerically obtained potential and fitted one from the parameter set A by the scaling rules.

The Skyrme model of a massless pion has one dimensionful parameter, F_π, and one coupling constant, e. These are scaled out by introducing the standard unit, where length is expressed by

$$y = eF_\pi r. \tag{31}$$

By using this, soliton profiles for various F_π and e are related by a simple scale transformation to each other. In Fig. 14, we show the soliton profiles as functions of the physical radial distance r for the three parameter sets A, B, and C, which are obtained from the standard profile function with the scaling rule Eq. (31). From Fig. 14, we find that the profile function for the set C is most extended among the three parameter sets; soliton size is inversely proportional to eF_π.

Having established the scaling rule for the soliton profile, let us investigate possible scaling rules for the antikaon nucleon potential. First, let us look at the relations among the parameter sets A, B, and C, and then we will discuss general cases.

As expected from a dimensional argument, it is shown that the range parameters for the parameter sets A and B, for instance, are related by

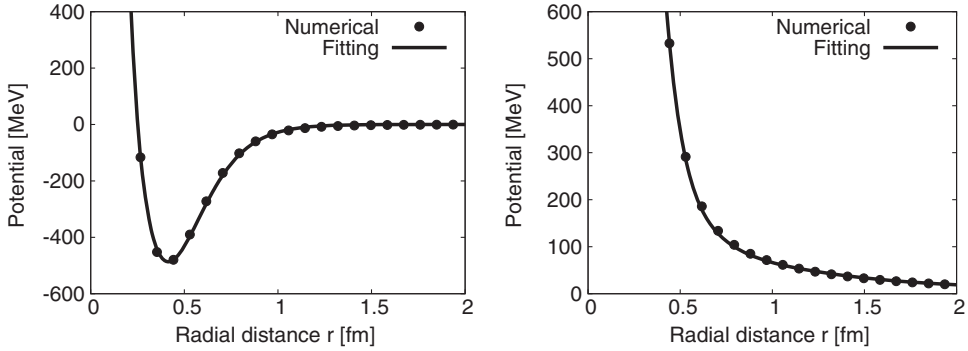

FIG. 15. Total potentials for the $\bar{K}N(J^P = 1/2^-, I = 0)$ channel from the bound state (left) and the $\bar{K}N(J^P = 3/2^+, I = 0)$ channel from a scattering state (right) for the parameter set B, which are derived from the potentials for the set A by the scaling rules Eqs. (32)—(34). The scattering energies are −32.2 and 27 MeV for s and p waves, respectively.

$$R^B = \frac{\alpha^A}{\alpha^B} R^A \tag{32}$$

for all components of the potential. Here, we have defined α as $\alpha = eF_\pi$, and the superscripts A and B correspond to the parameter sets A and B, respectively; namely, we take as follows: $\alpha^A = 4.67 \times 205\,\mathrm{MeV}$ and $\alpha^B = 4.82 \times 186\,\mathrm{MeV}$.

Contrary, interaction strengths obey differently for different components.

(i) For the components which do not include G_{-2} as a fitting function, $U_0^c(WZ, r)$, $U_\tau^c(N, r)$, $U_0^{LS}(N, r)$, $U_0^{LS}(WZ, r)$, and $U_I(r)$, the strength parameters are scaled by the following rules:

$$C_i^B = C_i^A, \qquad (i = -2, 0, 2). \tag{33}$$

(ii) For the others [$U_0^c(N, r)$ and $U_\tau^{LS}(N, r)$], they obey the different rule as follows:

$$C_i^B = \left(\frac{\alpha^B}{\alpha^A}\right)^2 C_i^A, \qquad (i = -2, 0, 2). \tag{34}$$

In Fig. 15, we have shown the potentials for the same channel as in Fig. 12 for the parameter set B. The s-wave potentials are calculated at the binding energy of the corresponding parameter set, namely, $\varepsilon = -32.2$ MeV. The p-wave potential is calculated at the common scattering energy $\varepsilon = 27$ MeV. From Figs. 15, we find that the potentials for the parameter set A is scaled into the set B with the scaling rules Eqs. (32)—(34) in a good manner. In Appendix D, we show the results for the set C.

Finally, we consider general parameter sets. To do that, let us first observe that the potential contains terms with different $1/N_c$ behaviors; the one originates from the soliton profile (leading order term) and the one from the rotation (higher order term). The former is factored out by 1 in the standard unit, while the latter by $e^3F_\pi \sim 1/N_c$, which is inversely proportional to the moment of inertia. Because of this, the scaling rules for different parameter sets of F_π and e differ for these two terms of different $1/N_c$ orders. For the case of the set A, B, and C, because the parameters are chosen to preserve the value of e^3F_π unchanged, we have obtained a simple scaling rule as dictated by Eqs. (32)—(34). In general, this is no longer the case, and we have to consider the scaling rules for the leading and higher order terms, separately. To see how the simple scaling rule holds in general, we introduce a new parameter set D, which is taken as $F_\pi = 186$ MeV and $e = 5.85$. In this parameter set, we set the pion decay constant at the experimental value, while the Skyrme parameter at the $\rho\pi\pi$-coupling constant, $g_{\rho\pi\pi}$, determined from the KSRF relation [35,36],

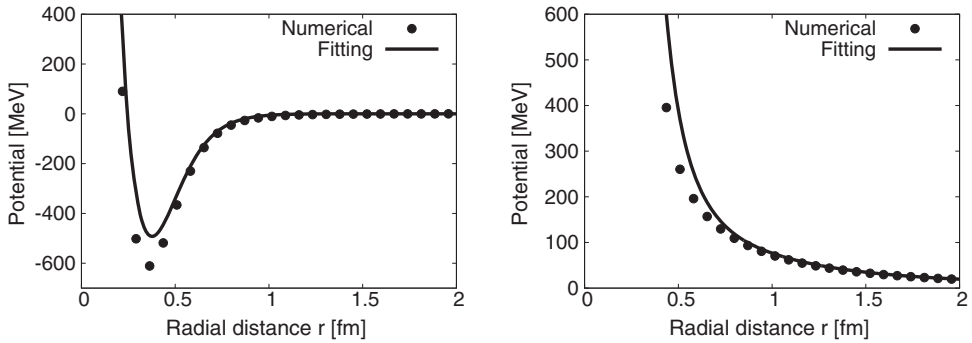

FIG. 16. Potentials for the $\bar{K}N(J^P = 1/2^-, I = 0)$ channel from the bound state (left) and the $\bar{K}N(J^P = 3/2^+, I = 0)$ channel from a scattering state (right) for the parameter set D, which are derived from the potentials for the set A by the scaling rules Eqs. (32)—(34). The scattering energies are −21.0 and 27 MeV for s and p waves, respectively.

$$m_\rho^2 = \frac{g_{\rho\pi\pi}^2 F_\pi^2}{2}, \tag{35}$$

where $m_\rho = 770$ MeV, which is the mass of the ρ meson. We show the potential calculated by the set D and those expected by the scalings Eqs. (32)—(34) in Fig. 16. The binding energy of the $\bar{K}N$ bound state is 21.0 MeV for the set D, and the scattering energy is for 27 MeV for the p wave. There is some deviation between the two, which is not, however, very large. To conclude this subsection, the potential obeys a simple scaling rule as long as the moment of inertia is unchanged.

V. SUMMARY

In this paper, we have discussed the (anti)kaon-nucleon scattering states and the (anti)kaon-nucleon potentials by a modified bound state approach in the Skyrme model, which is more suited to the study of the physical kaon and nucleon [6]. In our approach, the potential contains terms of different orders of $1/N_c$ due to the change of the order of the projection and variation. This violates the $1/N_c$ expansion series, but it is reasonable for physical systems of a weakly interacting (anti)kaon and nucleon, which may generate molecular like states.

First, we have investigated the phase shifts for the (anti) kaon-nucleon scattering with the lower partial waves of the (anti)kaon. The obtained phase shifts indicate that the potential is attractive for the $\bar{K}N$ channel and repulsive for the KN one. Then, we have evaluated the scattering length for the $\bar{K}N$ scattering state but it turns out to be larger than the experimental results and other theoretical calculations [29–33].

Second, to make further discussions for the potential, we have classified the $\bar{K}N$ potential into the seven components according to their natures with and without an energy dependence. Then, we have fitted them by the Gaussian type functions. As a result, we have found that all the components can be fitted by the Gaussian type functions. Actually, we have verified that the binding energies of the $\bar{K}N$ bound state and the phase shifts derived from the fitted potential and those from the numerically obtained original ones agree well.

While fitting the potential, we have also investigated the scaling rules associated with the soliton profile function, when changing the model parameters F_π and e. We have found that various components of the potential contain terms of a different order of $1/N_c$, which obey different scaling rules, separately. However, by keeping the moment of inertia in the higher order terms unchanged when F_π and e are varied, these separate scaling rules reduce to a simple rule for each component.

For further studies, it would be necessary to take into account the finite mass effect of the pion due to explicitly chiral symmetry breaking and the difference in F_π and F_K due to SU(3) flavor symmetry breaking. Furthermore, the coupling of $\bar{K}N$ and $\pi\Sigma$ is important. It was investigated in the Callan-Klebanov bound state approach [37]. However, the antikaon is not a physical one in their work. Improvements by considering these issues should be performed for more quantitative discussions of (anti) kaon-nucleon systems including $\Lambda(1405)$.

ACKNOWLEDGMENTS

We thank Noriyoshi Ishii for useful discussions. This work is supported in part by the Grant-in-Aid for Science Research Grant No. JP26400273(C) and JP17K05441(C).

APPENDIX A: THE EQUATION OF MOTION AND INTERACTIONS

In this appendix, we show the explicit expressions of various terms in the equation of motion Eq. (14),

$$-\frac{1}{r^2}\frac{d}{dr}\left(r^2 h(r)\frac{dk_l^\alpha(r)}{dr}\right) - E^2 f(r) k_l^\alpha(r) + (m_K^2 + V(r))k_l^\alpha(r) = 0, \tag{A1}$$

where

$$h(r) = 1 + \frac{1}{(eF_\pi)^2}\frac{2}{r^2}\sin^2 F, \tag{A2}$$

$$f(r) = 1 + \frac{1}{(eF_\pi)^2}\left(\frac{2}{r^2}\sin^2 F + F'^2\right), \tag{A3}$$

$$V(r) = V_0^c(r) + V_\tau^c(r) I_{KN} + V_0^{LS}(r) J_{KN} + V_\tau^{LS}(r) J_{KN} I_{KN}. \tag{A4}$$

In Eq. (A4), we define I_{KN} and J_{KN} as follows:

$$I_{KN} = \boldsymbol{I}^K \cdot \boldsymbol{I}^N, \qquad J_{KN} = \boldsymbol{L}^K \cdot \boldsymbol{J}^N, \tag{A5}$$

where the nucleon spin and isospin operators, $\boldsymbol{J}^N$ and $\boldsymbol{I}^N$, are given by [38]

$$\boldsymbol{J}^N = i\Lambda \mathrm{tr}[\boldsymbol{\tau}\dot{A}^\dagger(t)A(t)], \qquad \boldsymbol{I}^N = i\Lambda \mathrm{tr}[\boldsymbol{\tau}\dot{A}(t)A^\dagger(t)]. \tag{A6}$$

In Eq. (A6), $\dot{A}(t)$ is the time derivative of an isospin rotation matrix, $A(t)$, $\boldsymbol{\tau}$ are the 2×2 Pauli matrices, and Λ is the soliton moment of inertia given by [22],

$$\Lambda = \frac{2\pi}{3}F_\pi^2 \int dr r^2 \sin^2 F\left[1 + \frac{4}{(eF_\pi)^2}\left(F'^2 + \frac{\sin^2 F}{r^2}\right)\right]. \tag{A7}$$

The isospin and angular momentum operators of the kaon, $\boldsymbol{I}^K$ and $\boldsymbol{L}^K$, are given by

$$\boldsymbol{I}^K = \frac{\boldsymbol{\tau}}{2}, \qquad \boldsymbol{L}^K = \boldsymbol{r} \times \boldsymbol{p}^K, \tag{A8}$$

where $\boldsymbol{p}^K$ is the momentum of the kaon.

Finally, the explicit forms of each term in the interaction, $V(r)$, are given by the following equations:

$$V_0^c(r) = -\frac{1}{4}\left(2\frac{\sin^2 F}{r^2} + (F')^2\right) + 2\frac{s^4}{r^2} + \left[1 + \frac{1}{(eF_\pi)^2}\left(F'^2 + \frac{\sin^2 F}{r^2}\right)\right]\frac{l(l+1)}{r^2} - \frac{1}{(eF_\pi)^2}\left[2\frac{\sin^2 F}{r^2}\left(\frac{\sin^2 F}{r^2} + 2(F')^2\right) - 2\frac{s^4}{r^2}\left(F'^2 + \frac{\sin^2 F}{r^2}\right)\right] + \frac{1}{(eF_\pi)^2}\frac{6}{r^2}\left[\frac{s^4 \sin^2 F}{r^2} + \frac{d}{dr}\{s^2 \sin F F'\}\right] + \frac{2E}{\Lambda}s^2\left[1 + \frac{1}{(eF_\pi)^2}\left(F'^2 + \frac{5}{r^2}\sin^2 F\right)\right] + \frac{3}{(eF_\pi)^2}\frac{1}{r^2}\frac{d}{dr}\left[r^2\left(\frac{EF' \sin F}{\Lambda}\right)\right] \pm \frac{3}{\pi^2 F_\pi^2}\frac{\sin^2 F}{r^2}F'\left(E - \frac{s^2}{\Lambda}\right), \tag{A9}$$

$$V_\tau^c(r) = \frac{8E}{3\Lambda}s^2\left[1 + \frac{1}{(eF_\pi)^2}\left(F'^2 + \frac{4}{r^2}\sin^2 F\right)\right] + \frac{4}{(eF_\pi)^2}\frac{1}{r^2}\frac{d}{dr}\left[r^2\left(\frac{EF' \sin F}{\Lambda}\right)\right], \tag{A10}$$

$$V_0^{LS}(r) = \frac{1}{(eF_\pi)^2}\frac{2E \sin^2 F}{\Lambda r^2} \pm \frac{3}{F_\pi^2 \pi^2}\frac{\sin^2 F}{\Lambda r^2}F', \tag{A11}$$

and

$$V_\tau^{LS}(r) = -\left[1 + \frac{1}{(eF_\pi)^2}\left(F'^2 + 4\frac{\sin^2 F}{r^2}\right)\right]\frac{16s^2}{3r^2} - \frac{1}{(eF_\pi)^2}\frac{8}{r^2}\left[\frac{d}{dr}(\sin F F')\right], \tag{A12}$$

where

$$s = \sin(F(r)/2), \tag{A13}$$

and

$$F' = dF(r)/dr. \tag{A14}$$

The last terms of Eq. (A9) and Eq. (A11) are derived from the Wess-Zumino term, which is attractive for the $\bar{K}N$ potential and repulsive for the KN potential.

APPENDIX B: FITTING PARAMETERS

In this appendix, we show the fitting parameters discussed in Sec. IV B.

TABLE III. Fitting parameters for $u_0^c(N,r)$ and $v_0^c(N,r)$ for the s wave (top) and p wave (bottom).

	$G_{-2}(r)$	$G_0(r)$	$G_2(r)$
Range [fm]	0.165	0.254	0.368
$u_0^c(N,r)$ [MeV]	3320	2903	−579
$v_0^c(N,r)$ [MeV]	−2244	−6343	−499

	$G_{-2}(r)$	$G_0(r)$	$G_2(r)$
Range [fm]	0.298	0.292	0.300
$u_0^c(N,r)$ [MeV]	−3161	2185	−504
$v_0^c(N,r)$ [MeV]	2965	−3249	−1995

TABLE IV. Fitting parameters for $u_0^c(WZ,r)$ and $v_\tau^c(WZ,r)$.

	$G_0^{(1)}(r)$	$G_0^{(2)}(r)$
Range [fm]	0.264	0.378
$u_0^c(WZ,r)$ [MeV]	−677	−1207
$v_0^c(WZ,r)$ [MeV]	−3449	−985

TABLE V. Fitting parameters for $u_\tau^c(N,r)$ and $v_\tau^c(N,r)$.

	$G_0(r)$	$G_2(r)$
Range [fm]	0.248	0.491
$u_\tau^c(N,r)$ [MeV]	401	291
$v_\tau^c(N,r)$ [MeV]	401	291

TABLE VI. Fitting parameters for $u_0^{LS}(N,r)$ and $v_0^{LS}(N,r)$.

	$G_0^{(1)}(r)$	$G_0^{(2)}(r)$
Range [fm]	0.281	0.452
$u_0^{LS}(N,r)$ [MeV]	127	78
$v_0^{LS}(N,r)$ [MeV]	125	78

TABLE VII. Fitting parameters for $u_0^{LS}(WZ,r)$ and $v_0^{LS}(WZ,r)$.

	$G_0^{(1)}(r)$	$G_0^{(2)}(r)$
Range [fm]	0.228	0.353
$u_0^{LS}(WZ,r)$ [MeV]	−574	−728
$v_0^{LS}(WZ,r)$ [MeV]	574	728

TABLE VIII. Fitting parameters for $u_\tau^{LS}(N,r)$ and $v_\tau^{LS}(N,r)$.

	$G_{-2}^{(1)}(r)$	$G_{-2}^{(2)}(r)$
Range [fm]	0.245	0.566
$u_\tau^{LS}(N,r)$ [MeV]	−7930	−1465
$v_\tau^{LS}(N,r)$ [MeV]	7930	1465

TABLE IX. Fitting parameters for the centrifugal force.

	$G_0^{(1)}(r)$	$G_0^{(2)}(r)$
Range [fm]	0.404	0.700
$u_l(r)$ [MeV$^2\cdot$fm^2]	66226	6074
$v_l(r)$ [MeV$^2\cdot$fm^2]	−66228	−6074

APPENDIX C: FURTHER DISCUSSIONS FOR $\tilde{U}_0^c(N,r)$

Here, we make a further classification for the isospin independent central components from the normal term, $\tilde{U}_0^c(N,r)$, which contains nonlocal contributions. As we mentioned in Sec. IV B, we first decompose $\tilde{U}_0^c(N,r)$ into local and nonlocal components as Eqs. (C1), (C2), and (C3).

$$\tilde{U}_0^c(r) \simeq \tilde{U}_0^c(r) + \frac{\partial \tilde{U}_0^c(r)}{\partial \varepsilon}\Delta_E \equiv u_0^c(r) + v_0^c(r)\Delta_E, \Delta_E \equiv \varepsilon/2m_K, \quad \text{(C1)}$$

$$u_0^c(N,r) = u_0^c(N,\text{local},r) + u_0^c(N,\text{non},r), \quad \text{(C2)}$$

and

$$v_0^c(N,r) = v_0^c(N,\text{local},r) + v_0^c(N,\text{non},r), \quad \text{(C3)}$$

where the arguments *local* and *non* stand for the local and nonlocal contributions, respectively. The nonlocal contributions originate from the first- and second-order derivatives in Eq. (17). Furthermore, we decompose the nonlocal components into two parts according to the order of the derivatives as follows:

$$u_0^c(N,\text{non},r) = x_1(r)\frac{(k_l^\alpha)'(r)}{k_l^\alpha(r)} + x_2(r)\frac{(k_l^\alpha)''(r)}{k_l^\alpha(r)} \quad \text{(C4)}$$

and

$$v_0^c(N,\text{non},r) = y_1(r)\frac{(k_l^\alpha)'(r)}{k_l^\alpha(r)} + y_2(r)\frac{(k_l^\alpha)''(r)}{k_l^\alpha(r)}, \quad \text{(C5)}$$

where the prime symbols mean the derivative with respect to the radial distance r, that is

$$(k_l^\alpha)'(r) = \frac{dk_l^\alpha(r)}{dr}, \qquad (k_l^\alpha)''(r) = \frac{d^2k_l^\alpha(r)}{dr^2}. \quad \text{(C6)}$$

Next, we fit all the local components, $u_0^c(N,\text{local},r)$ and $v_0^c(N,\text{local},r)$, and the coefficients, $x^i(r)$ and $y^i(r), (i=1,2)$ in Eqs. (C4) and (C5), with several Gaussian type functions shown in Eqs. (C7)—(C10),

$$G_{-2}(r) = C_{-2}\frac{1}{r^2/{R_{-2}}^2}\exp\left(-\frac{r^2}{{R_{-2}}^2}\right) \quad \text{(C7)}$$

$$G_{-1}(r) = C_{-1}\frac{1}{r/R_{-1}}\exp\left(-\frac{r^2}{{R_{-1}}^2}\right) \quad \text{(C8)}$$

$$G_0(r) = C_0\exp\left(-\frac{r^2}{{R_0}^2}\right) \quad \text{(C9)}$$

$$G_1(r) = C_1\frac{r}{R_1}\exp\left(-\frac{r^2}{{R_1}^2}\right) \quad \text{(C10)}$$

as summarized in Table X. The resulting fitted parameters are summarized in Tables XI–XIII, and we compare numerically obtained and Gaussian-fitted potentials in Figs. 17–19.

TABLE X. Various components of $\tilde{U}_0^c(r,N)$ and the corresponding fitted functions. The functions $u_0^c(N,\text{local},r)$ and $v_0^c(N,\text{local},r)$ are for energy independent and dependent local components of $\tilde{U}_0^c(N,r)$. $x_i(r)$ and $y_i(r)(i=1,2)$ are coefficients of ith derivatives for energy independent and dependent local components of $\tilde{U}_0^c(N,r)$. The fitted functions $G_n(r)$ are also defined in Eqs. (C7)—(C10). Superscripts, (1) and (2) of $G_0^{(\cdot)}(r)$, indicate that fitting parameters are different for the functions.

$u_0^c(N,\text{local},r)$, $v_0^c(N,\text{local},r)$	$G_{-2}(r)+G_0(r)$
$x_1(r), y_1(r)$	$G_{-1}(r)+G_1(r)$
$x_2(r), y_2(r)$	$G_0^{(1)}(r)+G_0^{(2)}(r)$

TABLE XI. Fitting parameters for $u_0^c(N,\text{local},r)$ and $v_0^c(N,\text{local},r)$.

	$G_{-2}(r)$	$G_0(r)$
Range [fm]	0.205	0.629
$u_0^c(N,\text{local},r)$ [MeV]	5730	85.8
$v_0^c(N,\text{local},r)$ [MeV]	−5570	317

TABLE XII. Fitting parameters for $x^1(r)$ and $y^1(r)$.

	$G_{-1}(r)$	$G_1(r)$
Range [fm]	0.235	0.431
$x_1(r)$ [1]	−3.40	0.516
$y_1(r)$ [1]	3.40	−0.516

TABLE XIII. Fitting parameters for $x^2(r)$ and $y^2(r)$.

	$G_0^{(1)}(r)$	$G_0^{(2)}(r)$
Range [fm]	0.281	0.453
$x_2(r)$ [1/MeV]	-1.25×10^{-3}	-7.76×10^{-4}
$y_2(r)$ [1/MeV]	1.25×10^{-3}	7.76×10^{-4}

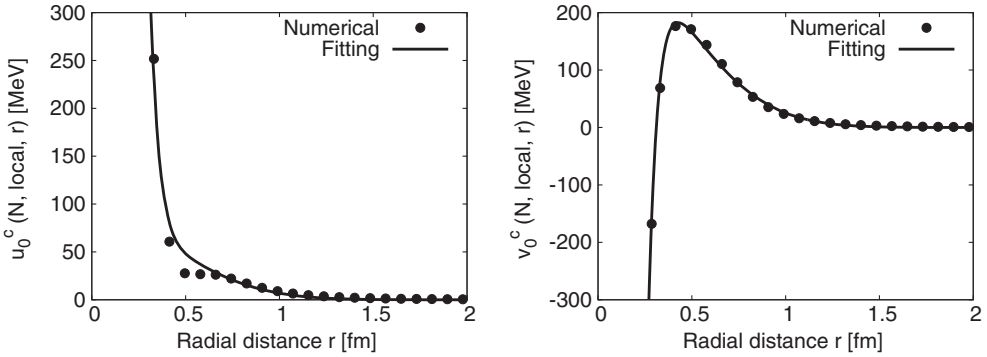

FIG. 17. Comparisons between the numerically obtained and the Gaussian-fitted potentials for the local components of $u_0^c(N, \text{local}, r)$ (left) and $v_0^c(N, \text{local}, r)$ (right).

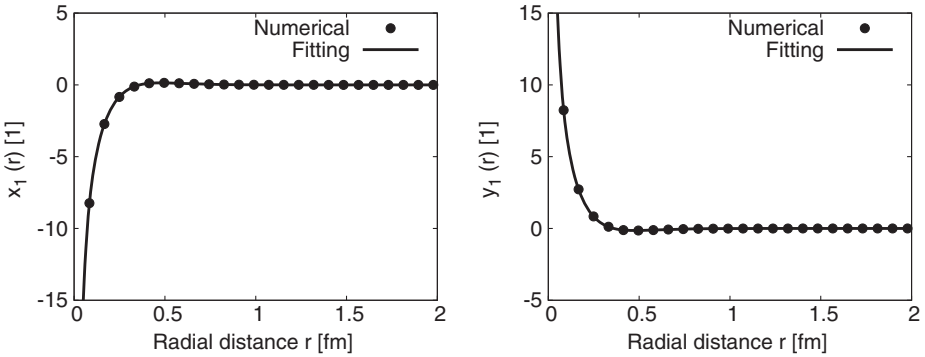

FIG. 18. Comparisons between the numerically obtained and the Gaussian-fitted coefficients for $x_1(r)$ (left) and $y_1(r)$ (right).

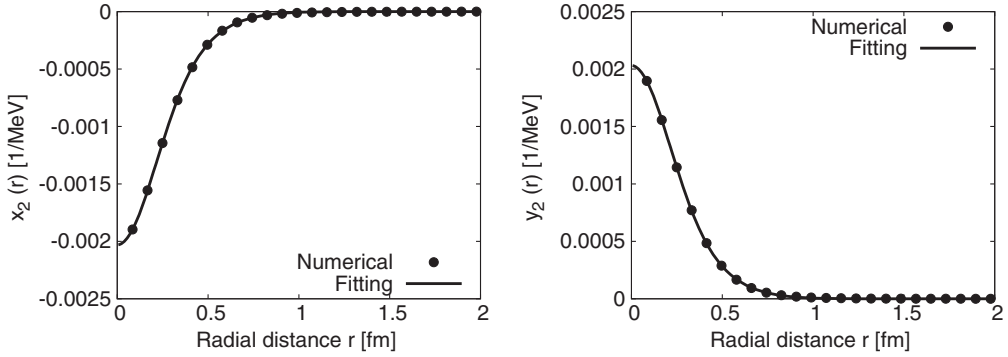

FIG. 19. Comparisons between the numerically obtained and the Gaussian-fitted coefficients for $x_2(r)$ (left) and $y_2(r)$ (right).

APPENDIX D: SCALING RULE FOR THE SET C

Following the discussions of the scaling rules in Sec. IV C, in this appendix, we scale the potential from the parameter set A to the set C with the scaling rules Eqs. (32)—(34). In Fig. 20, we show the numerically obtained and Gaussian-fitted potentials for the set C. As we mentioned in Sec. IV C, the s-wave potential ($J^P = 1/2^-, I = 0$) is calculated by using the bound state solution ($\varepsilon = -81.3$ MeV) and the p-wave potential ($J^P = 3/2^+, I = 0$) by a scattering state ($\varepsilon = 27$ MeV). From Fig. 20, we can conclude that the scaling rules work well for the parameter sets A and C.

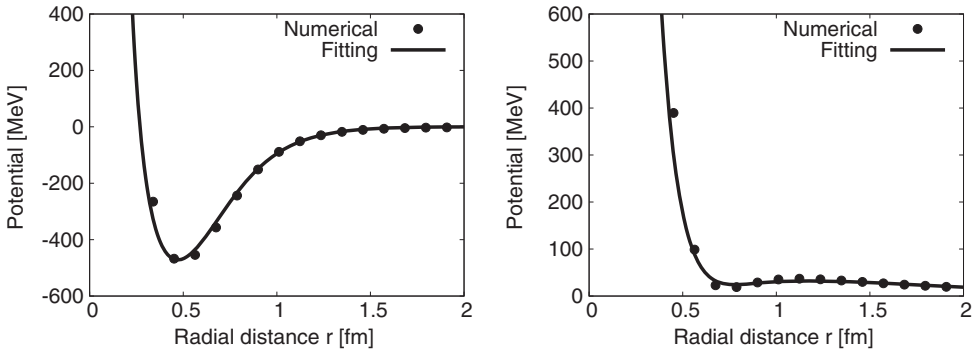

FIG. 20. Total potentials for the $\bar{K}N(J^P = 1/2^-, I = 0)$ channel from the bound state (left) and the $\bar{K}N(J^P = 3/2^+, I = 0)$ channel from a scattering state (right) for the parameter set C, which are derived from the potentials for the set A by the scaling rules Eqs. (32)—(34). The scattering energies are −81.3 and 27 MeV for s and p waves, respectively.

[1] R. H. Dalitz and S. F. Tuan, Phys. Rev. Lett. **2**, 425 (1959).
[2] R. H. Dalitz and S. F. Tuan, Ann. Phys. (N.Y.) **10**, 307 (1960).
[3] N. Isgur and G. Karl, Phys. Rev. D **18**, 4187 (1978).
[4] T. Yamazaki and Y. Akaishi, Phys. Lett. B **535**, 70 (2002).
[5] Y. Akaishi and T. Yamazaki, Phys. Rev. C **65**, 044005 (2002).
[6] T. Ezoe and A. Hosaka, Phys. Rev. D **94**, 034022 (2016).
[7] C. G. Callan, Jr. and I. R. Klebanov, Nucl. Phys. **B262**, 365 (1985).
[8] C. G. Callan, Jr., K. Hornbostel, and I. R. Klebanov, Phys. Lett. B **202**, 269 (1988).
[9] N. N. Scoccola, Phys. Lett. B **236**, 245 (1990).
[10] H. Walliser and H. Weigel, Eur. Phys. J. A **26**, 361 (2005).
[11] T. H. R. Skyrme, Proc. R. Soc. A **260**, 127 (1961).
[12] J. K. Perring and T. H. R. Skyrme, Nucl. Phys. **31**, 550 (1962).
[13] T. H. R. Skyrme, Nucl. Phys. **31**, 556 (1962).
[14] M. Praszalowicz, Phys. Lett. **158B**, 264 (1985).
[15] H. Yabu and K. Ando, Nucl. Phys. **B301**, 601 (1988).
[16] J. Wess and B. Zumino, Phys. Lett. **37B**, 95 (1971).
[17] E. Witten, Nucl. Phys. **B223**, 422 (1983).
[18] E. Witten, Nucl. Phys. **B223**, 433 (1983).
[19] V. B. Kopeliovich, B. Schwesinger, and B. E. Stern, Phys. Lett. B **242**, 145 (1990).
[20] B. Schwesinger and H. Weigel, Phys. Lett. B **267**, 438 (1991).
[21] V. B. Kopeliovich, B. Schwesinger, and B. E. Stern, Nucl. Phys. **A549**, 485 (1992).
[22] G. S. Adkins, C. R. Nappi, and E. Witten, Nucl. Phys. **B228**, 552 (1983).
[23] J. L. Rosner, S. Stone, and R. S. Van de Water, arXiv: 1509.02220.
[24] S. Weinberg, Phys. Rev. Lett. **17**, 616 (1966).
[25] Y. Tomozawa, Nuovo Cimento A **46**, 707 (1966).
[26] B. Moussallam and D. Kalafatis, Phys. Lett. B **272**, 196 (1991).
[27] B. Moussallam, Ann. Phys. (N.Y.) **225**, 264 (1993).
[28] In our previous paper [6], we reported that there was no bound state for the $I = 1$ channel with the parameter set B. After improving our numerical calculations, however, we have found a very shallow bound state with binding energy 0.2 MeV.
[29] M. Döring and U.-G. Meißner, Phys. Lett. B **704**, 663 (2011).
[30] B. Borasoy, U.-G. Meissner, and R. Nissler, Phys. Rev. C **74**, 055201 (2006).
[31] U. G. Meissner, U. Raha, and A. Rusetsky, Eur. Phys. J. C **47**, 473 (2006).
[32] G. Beer *et al.* (DEAR Collaboration), Phys. Rev. Lett. **94**, 212302 (2005).
[33] M. Iwasaki *et al.*, Phys. Rev. Lett. **78**, 3067 (1997).
[34] T. Fujiwara, T. Kugo, H. Terao, S. Uehara, and K. Yamawaki, Prog. Theor. Phys. **73**, 926 (1985).
[35] K. Kawarabayashi and M. Suzuki, Phys. Rev. Lett. **16**, 255 (1966).
[36] Riazuddin and Fayyazuddin, Phys. Rev. **147**, 1071 (1966).
[37] C. L. Schat, N. N. Scoccola, and C. Gobbi, Nucl. Phys. **A585**, 627 (1995).
[38] I. Zahed and G. E. Brown, Phys. Rep. **142**, 1 (1986).